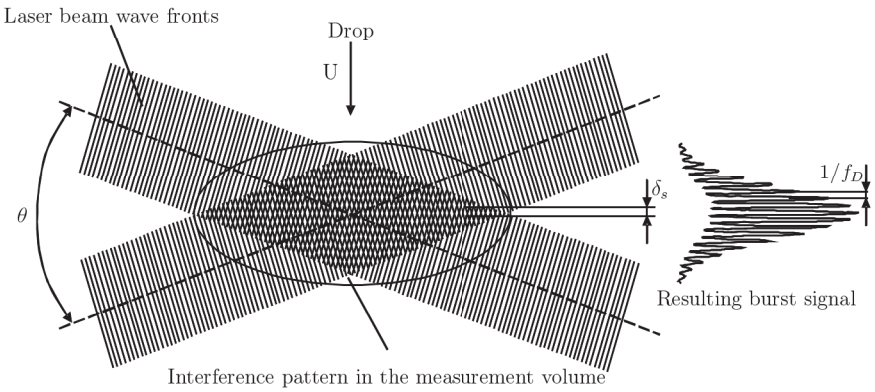

Figure 6.3: Interference fringe pattern of two intersecting laser beams and the resulting burst signal of a drop passing through the measurement volume

The working principle of the drop velocity measurements with *PDA* can be explained very well by using the fringe pattern shown in Figure 6.3. This simple fringe pattern model is based on the correct physical relations and is therefore presented here. The model is based on the fact that at the place where two laser beams with the same wavelength intersect with each other, a pattern of bright and dark interference planes appears. The appearance of this fringe pattern is based on the interference of the planar wave fronts of the two intersecting laser beams. One of the requirements for interference is that both intersecting laser beams are coherent. For *PDA* this requirement is satisfied, as both laser beams are emitted by one laser source, therefore having the same unique wavelength (i.e. monochromatic light). This laser beam is then split into two beams by passing through a beam splitter, after which, with the use of lenses, these two beams intersect in the desired measurement volume. In case of a relative phase shift between the two laser beams of 360°, the intensity at the intersection points is doubled, whereas a phase shift of 180° results in an extinction of the intensity. The resulting intensity pattern is shown in Figure 6.3.

From geometrical considerations the distance between the fringes δ_s can be determined with the following relation:

$$\delta_s = \frac{\lambda}{2 \sin \theta} \tag{6.1}$$

Here λ is the laser beam wavelength and θ is the intersecting angle of the two laser beams. A particle or a drop that crosses the intersection volume will scatter the laser light every time it passes through a bright interference band. By measuring the Doppler-frequency f_D of the intensity fluctuations of the scattered light, the particle or drop velocity component normal to the fringes, U_d, can be computed according to:

$$U_d = f_D \delta_s = \frac{f_D \lambda}{2 \sin \theta} \tag{6.2}$$

The Doppler-frequency is directly proportional to the absolute value of the velocity to be determined, but the direction of the measured velocity cannot be determined in this way, as the recorded signal is identical for two particles or drops moving in opposite directions. To overcome this directional ambiguity, the two incident beams are given different wavelengths. This

is achieved by shifting the frequency of one of the two laser beams by 40 MHz, making use of a Bragg cell. The graphical motivation for this measure is that the fringe pattern *moves* as one beam is shifted, resulting for a stationary particle in a signal with the shift frequency.

Provided that the scattering drops are spherical, the Doppler-signal cannot only be used for the drop velocity determination, but also for the drop diameter identification. The points where the incident laser beams make the first contact with the drop are called the "incident points", whereas the light recorded by the detectors comes only from small points on the surface of the drop, the so-called "glare points" (Albrecht *et al.* [1]). The properties of the drop, like the diameter, as well as the arrangements of the illumination source and the detector, determine the position of these incident and glare points. It has to be noted, that one incident and one glare point exist for each pair of incident laser beam and receiver.

In order to measure the drop diameter, more than one detector is needed to measure the scattered light in different directions. Each of these detectors measures the same Doppler-frequency. For very small particles, the glare points merge, due to which the signal for every detector will be the same, i.e. no phase shift will have taken place, as is sketched in the upper part of Figure 6.4.

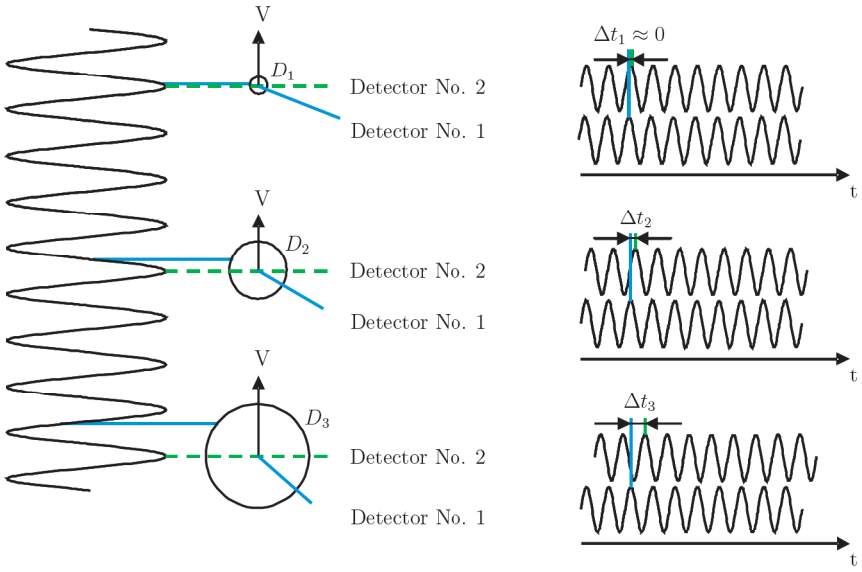

Figure 6.4: Principle of particle size determination

This is the lower boundary of particles that can be measured by the detectors, as there exists a linear relation between the drop diameter D_d and the phase shift Φ given by:

$$D_d = \frac{\Phi}{2\pi} \cdot \frac{\lambda}{\beta} \tag{6.3}$$

Here β is a function of the light scatter mechanism. When a drop scatters the light by reflection, the value of β is a function of the angle between the two interfering laser beams θ, the scattering angle ϕ and the angle between the different detectors ψ and is calculated as:

$$\beta = \frac{\sin\theta sin\psi}{\sqrt{2(1 - cos\theta cos\psi cos\phi)}} \tag{6.4}$$

In case of first order refraction, however, the refraction index n of the drop fluid has to be taken into account:

$$\beta = \frac{-n \sin\theta sin\psi}{2(1 + cos\theta cos\psi cos\phi)(1 + n^2 - n\sqrt{2(1 + cos\theta cos\psi cos\phi)})} \tag{6.5}$$

A noticeable phase shift between the signals occurs, however, for drops that are larger than the wavelength of the intersecting laser beams, as can be seen in the middle of Figure 6.4. The different detectors receive now signals that are coming from different glare points, which correspond to different incident points. This results in a different interference of the laser beams on each detector, which are measuring the same Doppler frequency, but in combination with a phase shift between the receiving signals. This phase shift is an increasing function of the size of the drop, as well as of the angle between the detectors, as can be seen by comparing the response functions for the three drop sizes in Figure 6.4.

For larger drop diameters the phase shift measured by a detector pair increases. However, two detectors cannot distinguish between a phase shift of Φ and $\Phi + 2\pi$. This results therefore in a phase ambiguity. To overcome this phase ambiguity, three detectors are being used, ordered in space at different elevation angles. In this way, two signal pairs are formed, one with a large angle and the other with a small angle. This leads to a large measurement range of the drop diameters, together with a high measurement accuracy. At the same time, for each measured drop, a comparison between the measured phase differences can be used to check the sphericity of each drop, in case this is required for the measurement.

Adaptation of *PDA*-technique to the measurement requirements

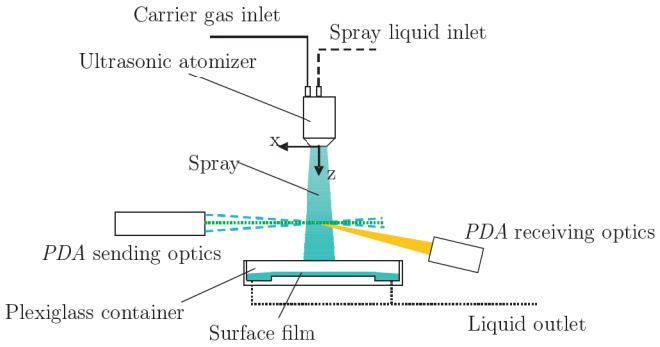

Figure 6.5: Layout of the *PDA*-technique for spray characterisation

For the measurements described hereafter, the commercial *PDA*-system manufactured by Dantec Dynamics is used. The equipment makes use of the blue (488 nm) and green (514.5 nm) lines of the Ar^+-laser, hence two velocity components are measured simultaneously. Each laser beam is split up into two separate beams, after which one beam of each color is shifted by 40 MHz, making use of a Bragg cell, to avoid the velocity direction ambiguity described above. The transmitting optics is equipped with a lens with a focal length of 600 mm and a distance between the laser beams of 38.75 mm is used. The unfocused laser beams have a diameter of 1.35 mm, leading to a measurement volume of 143 μm in diameter and 2.25 mm in length. The length of the measurement volume visible for the detectors is reduced by a mask to about 200

μm, resulting in a maximum measurable drop diameter of 321 μm. For the receiving optics a lens with a focal length of 500 mm is used and the angle between the transmitting and receiving optics, θ, equals 150°.

The setup for the *PDA* measurements is shown in Figure 6.5 and in Figure 6.6 for, respectively, the side and top view.

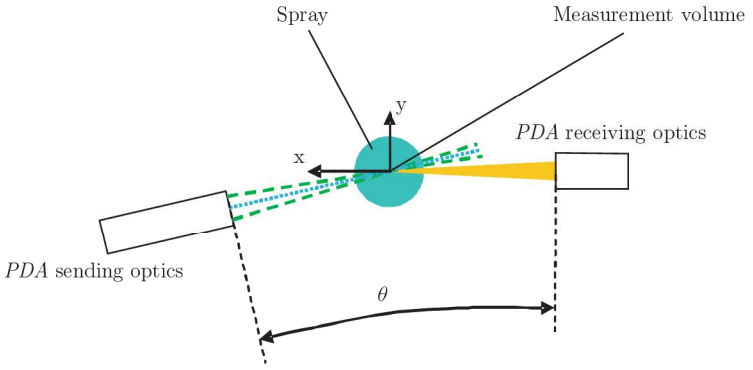

Figure 6.6: Layout of the *PDA*-technique for spray characterisation, seen from above

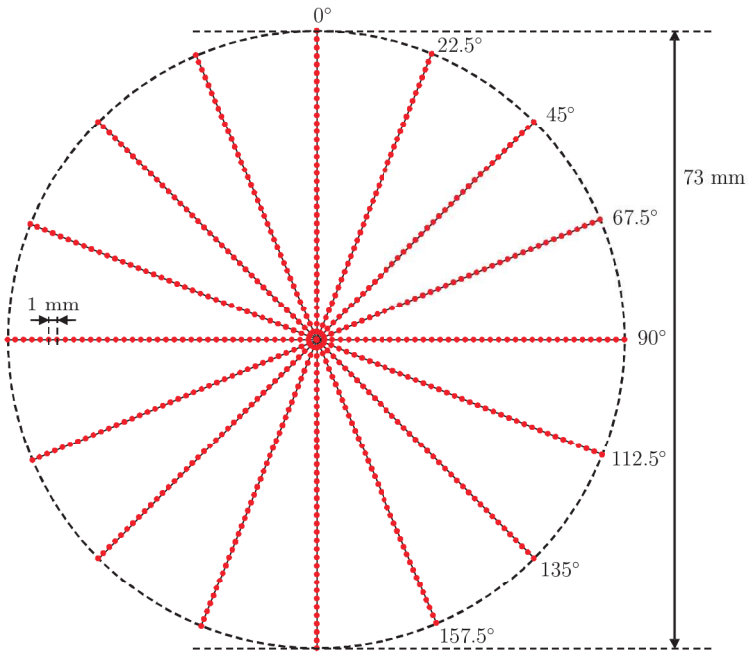

Figure 6.7: Measurement grid for PDA measurements

For each investigated nozzle, *PDA*-measurements at two different measurement heights (z = 48.8 mm and z = 110 mm for US10, and z = 61.3 mm and z = 122.5 mm for US20) are conducted. At each height inside the spray, a grid in eight radial directions is measured, i.e. from 0° to 180° in steps of 22.5°. Along each of these lines, 73 measurement points are being laid, 36 in each direction seen from the center of the circular measurement grid, with a step size of 1 mm between the different points, see Figure 6.7. This results in 568 measurement points per investigated height in the spray. At each measurement position the velocity component

in the z-direction and the drop diameter, with a pre-set spherical validation of $\pm$ 10 %, are recorded for at least 5000 drops.

6.2.2 Particle Image Velocimetry

Working principle

Particle Image Velocimetry (PIV) is an optical measurement technique to quantitatively resolve, in its basic version, the flow velocity over a planar domain. For a detailed overview of this measurement technique see for example Raffel *et al.* [124]. PIV is a non-intrusive method, based on laser light scattering by tracer particles, to capture the instantaneous velocity field. The basic idea of the PIV-technique consists in the evaluation of the instantaneous fluid velocities, by recording the position of the images of tracer particles suspended in the fluid at successive time instants by a CCD camera: two successive images of tracer particles, illuminated by a light sheet, are acquired within a short time-interval of several microseconds to several milliseconds between them, depending on the pre-estimated absolute velocity of the studied fluid. These images are recorded either on a single frame or on a sequence of frames. The resulting image pairs, taken in a known time interval, provide a displacement record of the tracer particles within the measurement plane, which is then analysed and scaled to the fluid velocity. The velocity information produced in this way tends towards the true instantaneous velocity distribution at a certain time instant when the laser pulse separation and the camera exposure time are smaller than the smallest time scales of interest in the studied flow.

Seeding particles are introduced into the flow in order to reveal the motion of the fluid. They must accurately follow the flow, while scattering sufficient light to be detectable, which leads to small tracer particles for the first consideration and large sized particles for the second consideration. For qualitatively and quantitatively good results a balance between these two considerations is required. It is clear that by measuring the tracer particle velocity instead of the fluid velocity, PIV is an indirect measurement technique. Therefore, the fluid mechanical properties of the tracers have to be considered to avoid significant differences between the tracer and the fluid motion. The acceleration of the flow and its interaction with the possible investigated object is followed with a time lag by the tracer particles. The velocity difference between the particles and the surrounding flow is given by:

$$\overline{U}_s = \overline{U}_p - \overline{U} = d_p^2 \frac{(\rho_p - \rho)}{18\mu} \overline{a} \tag{6.6}$$

Here, $\overline{U}_p$ is the absolute particle velocity, $\overline{U}_s$ the absolute slip velocity and $\overline{a}$ is defined as $\overline{a} = \frac{d\overline{V}}{dt} + \overline{g}$.

If the density of the tracer particles is much larger than the fluid density, the slip velocity $\overline{U}_s$ typically follows an exponential law:

$$\overline{U}_s = -\overline{U} \cdot e^{-t/\tau_s} \tag{6.7}$$

Here, τ_s is the relaxation time defined as

$$\tau_s = d_p^2 \frac{\rho_p}{18\mu} \tag{6.8}$$

This relaxation time is a measure of how well the particles follow rapid changes in the velocity direction and magnitude. For the current measurements of the velocity distributions inside the surface film during spray impingement, described in next section, the tracer particles have the following characteristics: $d_p = 10\mu m$, $\rho_p = 1.19 g/cm^3$ and $\mu = 2.3 \cdot 10^{-3} kg/(m \cdot s)$. This leads to a relaxation time of 2.9 μs, which is much smaller than the lowest times scales (80 μs) associated with the spray impingements described hereafter. This proves that the particles used follow the flow fluctuations inside the surface film very well.

If plain light waves impinge on an opaque screen containing a circular aperture, they generate a far-field diffraction pattern on a distant observing screen. In a camera, the lens makes sure that the far-field pattern can be imaged on an image sensor close to the aperture without any changes. However, the small imaged scattering particle inside the light sheet does not appear as a point in the image plane, but forms a so-called Fraunhofer diffraction pattern. A circular pattern, which is known as the Airy disk, will be obtained for a low exposure. Surrounding Airy rings can be observed for a very long exposure. The diameter of the Airy disk, d_{diff}, represents the smallest particle image that can be obtained for a given imaging configuration. This diameter is defined as:

$$d_{diff} = 2.44 f_\sharp (M + 1)\lambda \tag{6.9}$$

Here, $f_\sharp$ is the f-number defined as the ratio between the focal length f and the aperture diameter D_a and M the magnification factor defined as the ratio between the geometric distance from the lens center till the image plane, z_0, and the distance between the object plane and the center of the lens, Z_0.

In PIV this minimum image diameter d_{diff} will only be obtained when recording small particles, in the order of a few microns, at small magnifications. For larger particles and/or larger magnifications the influence of geometric imaging becomes more and more dominant. The image of a finite-diameter particle is given by the convolution of the point spread function with the geometric image of the particle. If lens aberrations can be neglected and the point spread function can be approximated by the Airy function, the following formula can be used for an estimate of the particle image diameter:

$$d_\tau = \sqrt{(M d_p)^2 + d_{diff}^2} \tag{6.10}$$

The minimum image diameter which can be obtained due to diffraction, is commonly used also as the acceptable diameter of the geometric image. Therefore the particle image diameter obtained with equation (6.10) can be used to estimate the depth of field δ_z using the following equation:

$$\delta_z = 2 f_\sharp d_{diff} \frac{(M + 1)}{M^2} \tag{6.11}$$

It can be seen that a large aperture diameter is needed to get sufficient light from each individual particle within the light sheet and to get sharp particle images, because the size of the diffraction pattern can be decreased by increasing the aperture diameter. Unfortunately, a large aperture diameter yields a small diffraction spot diameter, which is a significant problem when imaging small tracer particles.

Fluorescent tracer particles are often used for multi-phase flows like sprays, as in this case not the light scattered by the tracer particles is recorded, but their fluorescence. This emitted fluorescent light has a different wavelength than the incident laser light, due to which it can be separated with a color filter from the light scattered by the drops, that has the same wavelength

as the incident laser light.

Once the images of the tracer particles have been recorded, the displacement information can be extracted. In order to extract this information, usually one of the two statistical approaches of PIV data processing, namely *auto-correlation* or *cross-correlation*, is applied. The main objective of statistical evaluation of PIV recordings is to determine the displacement between two patterns of particle images, which are stored as a two-dimensional distribution of grey levels. The difference between auto-correlation and cross-correlation is that auto-correlation is used for double exposed images, where the two subsequent positions of the particles are recorded in one image. This technique has a limited dynamic range and a 180° directional ambiguity, whereas the cross-correlation technique is used for single exposure images, therefore having a higher dynamic range and no directional ambiguity.

In Figure 6.8 the principle of the cross-correlation technique is shown.

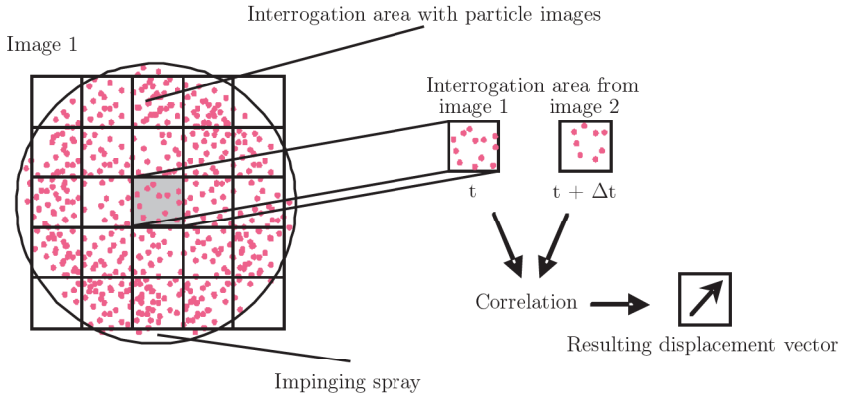

Figure 6.8: Determination of the displacement vector inside an interrogation area

In this figure, the cross-correlation between two interrogation windows out of the recordings is calculated. The two images are recorded a short time interval Δt apart. The intensity at a location (x, y) in image 1 is given by:

$$I_1(x,y) = P(x,y) \otimes \sum_{i=1}^{N} \delta(x - x_i(t_1), y - y_i(t_1)) \tag{6.12}$$

and the intensity in image 2 by:

$$I_2(x,y) = P(x,y) \otimes \sum_{i=1}^{N} \delta(x - x_i(t_2), y - y_i(t_2)) \tag{6.13}$$

Here, $P(x,y)$ is the intensity distribution for an individual particle image, (x_i, y_i) the initial coordinate for the i^{th} image, $x_i(t_2) = x_i(t_1) + u_i \Delta t$ and $y_i(t_2) = y_i(t_1) + v_i \Delta t$ and u_i and v_i the velocity components in the measurement plane. Each particle is assumed to have moved a mean distance of $s - \sqrt{x_0^2 + y_0^2}$. The two images are then subdivided into small interrogation windows and in each pair of interrogation windows the cross-correlation peak of $I_1(x,y)$ and $I_2(x,y)$ are determined by making use of the inverse Fourier Transform:

$$R_{I_1 I_2}(\varsigma, \eta) = \int_{-\infty}^{\infty} \int_{-\infty}^{\infty} I_1(x,y) \cdot I_2^*(x - \varsigma, y - \eta) dx dy \tag{6.14}$$

The distance from the origin (x_0, y_0) to the highest correlation peak indicates the average particle displacement across the subregion. In this way, no problems of a directional ambiguity arise.

In Chapter 2 the particle velocimetry measurement techniques for obtaining the third velocity component have been divided into two groups: those who calculate the three components of the velocity in a two-dimensional domain and those who determine the three-dimensional velocity inside a three-dimensional domain. For the second group of these measurement techniques, a volume laser illumination is required. Figure 6.9 shows the volume PIV illumination principle compared to the standard PIV.

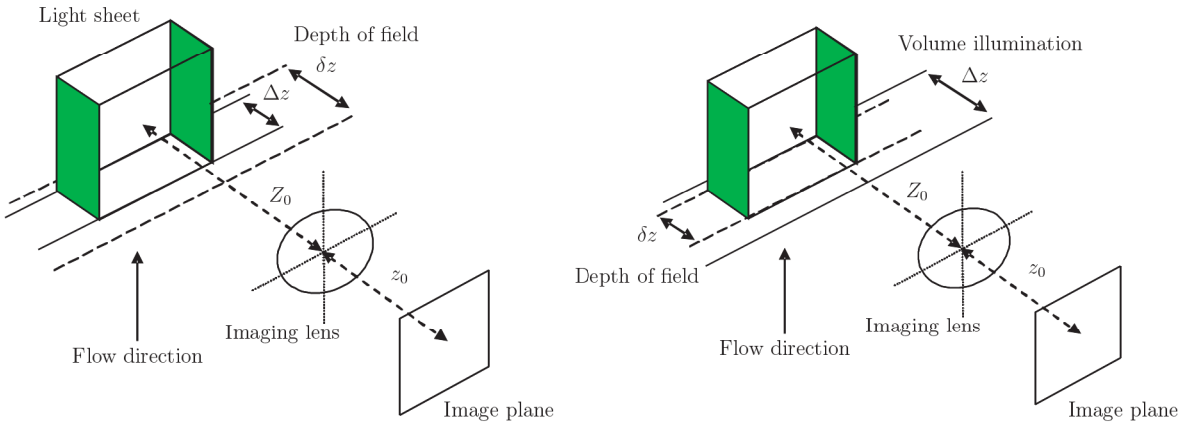

(a) Standard two-dimensional PIV (b) Volumetric micro-PIV

Figure 6.9: Comparison of standard two-dimensional PIV (left) and volumetric micro-PIV (right)

For standard PIV (left image in Figure 6.9) a quasi-two-dimensional light sheet illuminates the tracer particles. The depth of focus of the recording lens, δz, is much larger than the thickness of the laser light sheet, Δz. In this way, the depth of the measurement volume, Δz_0, is defined by the thickness of the light sheet. For PIV volume illumination either a very thick laser sheet is used ($\sim$ 2 - 5 mm) or the laser beam is expanded in diameter and passes orthogonally through the measurement area, as is the case for micro-PIV (μ-PIV), Meinhart *et al.* [95] and [96]. In this case, the depth of focus of the camera lens, δz, defines the depth of the measurement volume, Δz_0. The disadvantage of the volume illumination technique, however, is that out-of-focus particles still appear on the recorded images as blurred particles. For μ-PIV microscopic lenses are being used with very sharp edges of the focal plane, thereby partially compensating for the out-of-focus particles. When making use of a long distance microscope, there does not exist a sharp edge for the focal plane, resulting in out-of-focus particles having the same intensity as in-focus particles, hence, they form an important error source. Lindken *et al.* [85] have solved this problem using a light sheet having exactly the same thickness as the depth of focus of the long distance microscope. In this way out-of-focus particles are no longer illuminated. The problem of this technique, however, is that both light sheets have to overlap perfectly. The subsequent recording and analysis of the images by using the auto- or cross-correlation techniques is for a volume illumination PIV system exactly the same as has been described above for the standard PIV system.

Adaptation of *PIV*-technique to the measurement requirements

The PIV-measurement technique is used for the radial velocity analysis of the wall film produced by an impinging spray. The experimental setup is the same as has been described for the PDA-measurements, see §(6.2.1). The layout for the radial velocity measurements is shown in Figure 6.10.

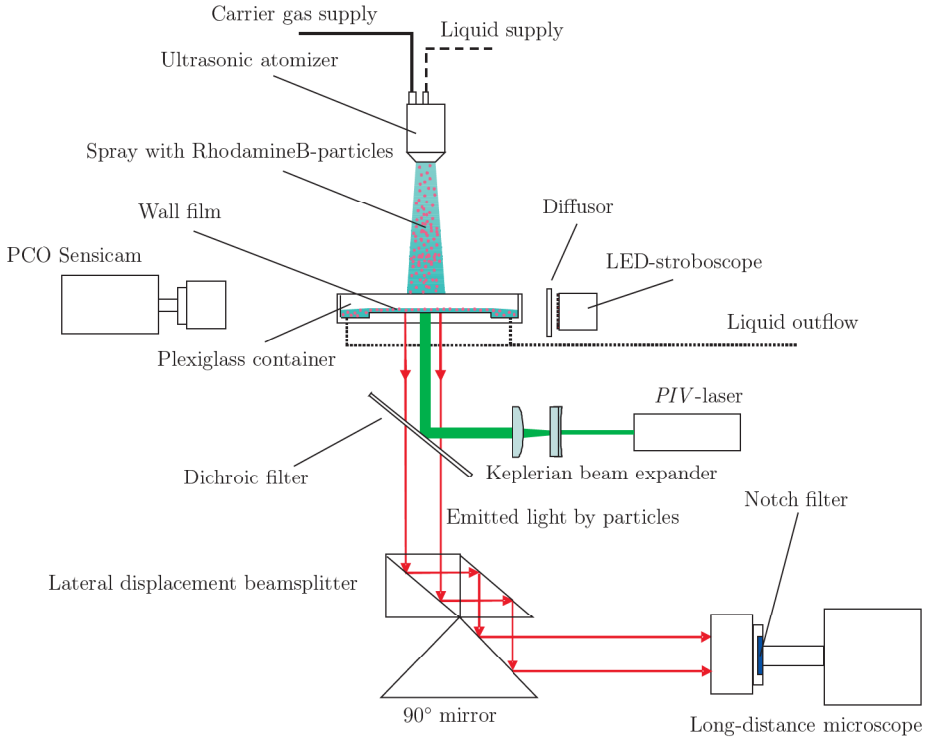

Figure 6.10: Layout of the volumetric *PIV*-technique for film radial velocity measurements

For the illumination, the same system is built as used on micro-scale in a μ-PIV system by making use of a microscope and a volume illumination to measure the different velocity components. The beam of the Spectron Dual SL404 Twin pulsed Nd:YAG laser - having a wavelength of 532 nm and an energy of 100 mJ/pulse with a pulse duration of 15 ns - is first expanded in diameter from 3 mm to about 12 mm by making use of a Keplerian beam expander with one plano-concave lens of -40 mm focal length and one of +150 mm. This expanded beam is diverted 90° upwards by a dichroic filter placed under 45°. This filter reflects wavelengths in a bandwidth of 535 nm $\pm$ 15 nm up to about 98 % and transmits the remaining wavelengths. The diverted beam illuminates in this way a vertical column of target liquid of 12 mm diameter.

The liquid of the spray (a mixture of 70% water and 30% glycerine) is mixed with 10 μm RhodamineB PMMA fluorescence particles, having a density of 1.19 g/cm^3. Different fluoresent particle types have been tested before the actual measurements, 4 μm Melaninresin particles with a density of 1.51 g/cm^3, 10 μm Polystyrene particles (1.09 g/cm^3) and 10 μm PMMA particles, but it was found that the PMMA particles give the best results when taking into account the relative density and the fluorescence intensity. Fluorescence particles are being used to avoid reflections on the drops and target film surface by the laser, as these particles emit light at a wavelength of 584 nm when illuminated by green laser light. This emitted light

passes through the dichroic filter, whereas the reflected laser light is blocked. A small part of the reflected laser light, however, will still pass through the dichroic filter, because 100 % reflection is only possible when the laser reflections hit this filter perpendicular. Therefore, a long-pass Raman filter, having a transmission bandwidth between 544 nm - 1200 nm is placed inside the lens of the camera in order to filter out about 99 % of the laser light reflections. A lateral displacement beam splitter in combination with a 90° mirror is used to divert the emitted laser light to the horizontal camera plane. One PCO Sensicam 12-bit CCD camera with 1280 × 1024 pixels is used to record the tracer particle images, equipped with a long distance microscope (Nikon Nikkor 105 mm focal length lens together with a 160 mm extension tube). This optical system results in a spatial resolution of 8.9 $\mu m/pix$, hence, a total field of view of 11.4 × 9.1 mm.

Figure 6.11 shows the PIV-setup seen from above, together with the measurement area that is being studied. One quarter of the total spray impingement region is selected to investigate the radial film velocity, with a total size of 44.4 × 45.1 mm. This region is subdivided into 20 equal areas of 11.4 × 9.1 mm; hence, the field of view of the recording camera, with an overlap of 0.4 mm and 0.1 mm respectively between two subregions. To get reliable data for the mean velocity components and their fluctuations, 1000 tracer particle image pairs are recorded per subregion at a recording rate of 2 Hz. The pulse separation time for each image pair is set variable between the different subregions, in order to capture also the slow moving particles at the edges of the investigated impingement region. This value varies between 80 μs and 14,000 μs, depending on the nozzle used, as well as on the volume flow and the use of the pressurized air as carrier gas. The operating conditions for the different measurements are shown in Table 6.1 in §(6.1).

Image processing of PIV-recordings

The image processing is done by making use of a PIV-algorithm (*WIDIM*) of the Technical University Delft, which was developed by Scarano [146]. To remove all the background noise in the images, the mean image intensity over the 1000 images per subregion is calculated. In this way, particles who stick to the bottom of the plexiglass container and do not move due to the no-slip condition at the wall are becoming visible. By applying background subtraction, these particles disappear, resulting in less possible local errors in the cross correlation algorithm. The main image analysis is subsequently carried out by the *WIDIM*-algorithm, making use of window deformation and iterative multi-grid cross-correlation. With this algorithm, the tracer particle images are analysed using final interrogation window sizes of 64 × 64 pixels and an overlap factor of 50%, yielding a measurement grid with a spatial resolution of 32 pixels, corresponding to approximately 1.1 mm. In this way, each tracer particle image generates an instantaneous vector field of 40 × 32 vectors.

After having analysed all the images for all the 20 subregions of spray impingement, 20 instantaneous vector fields, i.e. one for every subregion, are put together in such a way, that an vector field is generated, having the same dimensions as the original measurement area, hence 44.4 × 45.1 mm. Like this, 1000 total instantaneous vector fields with 155 × 156 vectors appear per nozzle operating setting, out of which the mean vector field and its fluctuations are being calculated. Post-processing tools are applied to receive the final velocity fields (eq. (6.15)) and their fluctuations (eq. (6.16)), as well as the turbulence intensity (eq. (6.17)).

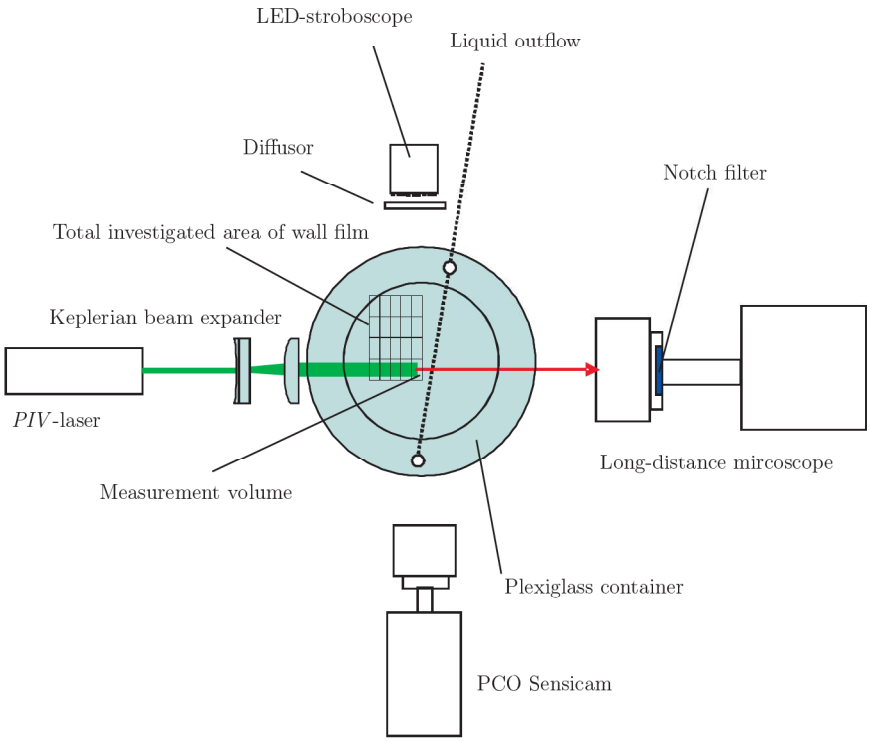

Figure 6.11: Measurement positions for the radial wall film velocity determination using volumetric *PIV*, seen from above

$$\overline{u} = \frac{\sum_{i=1}^{N} u_i}{N} \qquad \overline{v} = \frac{\sum_{i=1}^{N} v_i}{N} \tag{6.15}$$

$$\overline{u'u'} = \sqrt{< u'u' >} = \frac{\sqrt{\sum_{i=1}^{N} (u_i - \overline{u})^2}}{N}$$

$$\overline{v'v'} = \sqrt{< v'v' >} = \frac{\sqrt{\sum_{i=1}^{N} (v_i - \overline{v})^2}}{N}$$

$$\overline{u'v'} =< u'v' >= \frac{\sum_{i=1}^{N} (u_i - \overline{u})(v_i - \overline{v})}{N} \tag{6.16}$$

$$TI = \sqrt{\overline{u'u'}^2 + \overline{v'v'}^2} \tag{6.17}$$

6.3 Summary

In this chapter the experimental arrangement designed to investigate the spray impingement process has been presented. In order to visualise clearly the impingement outcomes, an experimental arrangement has been presented in §(6.1).

Different measurement techniques have been described to account for the acquisition of several measurement parameters, like the time evolution of the cavity after drop impingement by Shadowgraphy §(3.2), the spray characteristics by phase-Doppler anemometry §(6.2.1) and the radial film velocity components by particle image velocimetry §(6.2.2). Of each of these measurement techniques, the working principle has been explained, followed by the adaptation of each technique to the experimental arrangements in order to acquire the desired measurement data. When applicable, the associated data analysis and post-processing have been presented as well.

Chapter 7

Film dynamics in spray impingement onto a wetted surface

The idea of the experiments presented in this chapter is to investigate the radial velocity field of the surface film, present on the target surface during spray impingement. Spray, impinging on a surface, generates on it an unsteady and wavy surface, due to the simultaneous and subsequent impingements of single spray drops. The velocity distributions inside this surface film are of great importance, for example in spray cooling. Here, the directions and magnitudes of these velocities give an indication in which direction and how fast the heat is being transported away from the hot surface, which parts of the hot surface are being cooled less and how fast the warm liquid is being refreshed by new cold liquid.

In order to interpret the velocity fields correctly, the spray has to be characterised. This is done by using two different measurement techniques, *PDA*, described in §(6.2.1) and used for the characterisation of the velocities and diameters of the drops of the spray before impingement, and *Shadowgraphy*, to obtain the shape of the spray cone, described in §(3.2). The results obtained with these two measurement techniques will be outlined in §7.1. The radial velocity distributions are measured using the particle image velocimetry technique, of which the optical arrangement and the adaptation of this technique to the measurement requirements are described in §(6.2.2). The velocity fields obtained for the different parameters, i.e. impingement height, volume flow and nozzle, are discussed in detail in §(7.2).

7.1 Spray characterisation by means of Shadowgraphy and PDA

The characterisation of the impinging spray is necessary for understanding the outcomes of the radial velocity measurements inside the surface film. With the shadowgraphy technique the shape of the spray cone can be determined, after which horizontal slices can be made at the exact distance from the nozzle corresponding to the investigated impingement heights. Out of these slices a measure for the impingement areas of the spray at the different impingement heights can be determined. These impingement areas are then compared with the results obtained with the phase-Doppler technique and the film velocity measurement data, to assign the exact influencing areas of the impinging sprays.

With the phase-Doppler technique the diameter and vertical velocity magnitude of each single drop of the spray, passing the measurement volume, can be determined, see §(6.2.1).

These data give an indication of the areas in the spray where large drop velocities and/or large drop diameters are present, resulting in more energetic impingements on and larger cavities inside the target surface film. These results are, for example, very interesting when applying the investigated ultrasonic nozzles for spray cooling, since energetic impingements generate larger velocity fluctuations and deeper cavities inside the surface film, therefore removing the heat from the hot surface at shorter time scales.

7.1.1 Spray cone measurements using shadowgraphy

As has been mentioned in §(6.1), two different ultrasonic nozzles of Lechler GmbH are being used, US10 and US20. The US10 atomizer has a working volume flow range between 1 and 10 L/h, the US20 nozzle between 2 and 20 L/h. Both nozzles are applied with and without carrier gas - here pressurized air with an overpressure of 0.604 bar - to investigate the influence of a stabilized spray on the film radial velocities. The operating conditions for the shadowgraphy measurements have been given in Table 6.1.

Figure 7.1 shows exemplary the shadowgraph images of the mean spray cone out of 500 recordings for the ultrasonic nozzle US10. In this Figure the left column represents the mean spray cone when no carrier gas is switched on, the right column shows the images where pressurised air under 0.604 bar overpressure is applied. The horizontal axis in the images is the radius, whereas the vertical axis represents the distance traveled from the nozzle. The two horizontal interrupted lines represent the two heights, at which the PDA-measurements §(7.1.2) as well as the PIV-measurements for the film radial velocity §(7.2) are conducted. These shadowgraph images give a clear qualitative overview of how to adjust the measurement systems (PDA and PIV) for spray and surface film flow characterisation.

Without applying the carrier gas (Figure 7.1, left column) it can be seen that for the lowest volume flow, here 50 mL/min, only a small mean spray cone is present, having a conical shape that changes only slightly in diameter. As the volume flow is increased up to 200 mL/min, the shape of the mean spray cone changes from a conical to a bell-shaped form. The same behaviour is found for the US20 nozzle for an increasing volume flow from 100 mL/min to 300 mL/min. When the pressurised air is applied, a completely different influence of the volume flow on the shape of the mean spray cone is seen, as the pressurised air stabilizes the spray cone. For increasing volume flows the diameter of the bell shape of the spray decreases, as the spray becomes more stable. This stabilising process can be explained by the two outer cores that are seen to be situated right after the nozzle exit, close to the outer border of the spray cone. This means that in case of applying the carrier gas, a hollow spray cone is obtained. For higher volume flows the outer cores move more to the inside, hence they get closer to the vertical rotational axis, and simultaneously increase in length. This length increase results in a stronger influence of the outer cores on the spray further downstream, therefore stabilizing the spray cone at positions downstream.

7.1.2 Spray drop characterisation using phase-Doppler measurements

In the last paragraph exemplary results of the mean shapes of the spray cones for the four different investigated volume flows for both ultrasonic nozzles have been presented. These results give a clear overview of the expected cone diameters at the two heights inside the spray at which the PDA- and PIV-measurements are conducted, hence a clear indication of where to position these different measurement techniques.

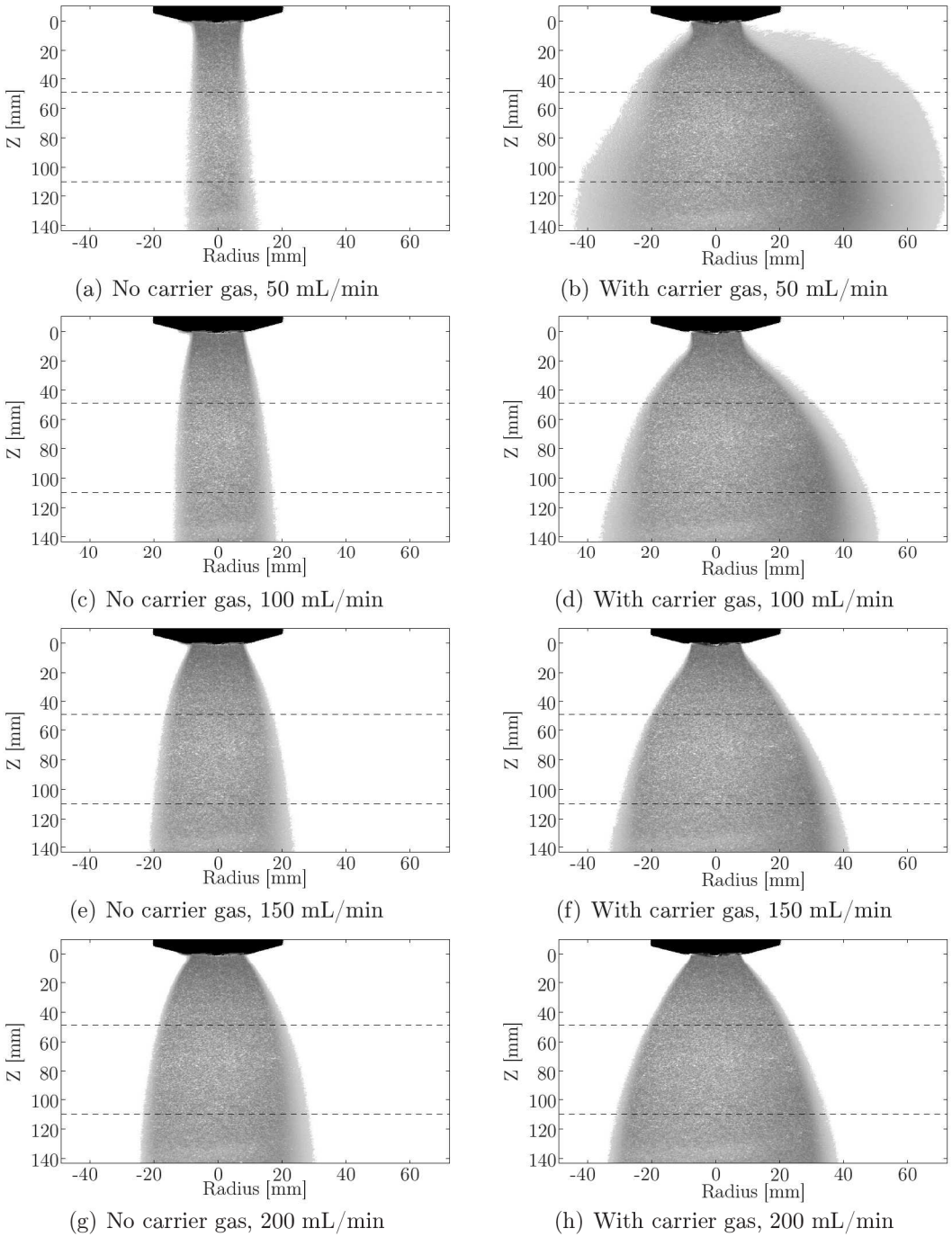

(a) No carrier gas, 50 mL/min

(b) With carrier gas, 50 mL/min

(c) No carrier gas, 100 mL/min

(d) With carrier gas, 100 mL/min

(e) No carrier gas, 150 mL/min

(f) With carrier gas, 150 mL/min

(g) No carrier gas, 200 mL/min

(h) With carrier gas, 200 mL/min

Figure 7.1: Shadowgraph images of the spray cone for the ultrasonic US10 nozzle, without (left) and with (right) pressurized air at 0.604 bar for different volume flows between 50 mL/min and 200 mL/min

This paragraph gives an overview of the results obtained with the phase-Doppler measurement technique. With this technique the diameter and two velocity magnitudes of each single drop of the spray, that passes the measurement volume, are determined. When averaged over time and space, the temporal and spatial distributions of the Sauter mean diameter, D_{32}, defined as the diameter of a sphere that has the same volume to surface area ratio as all measured drops, and the kinetic energies of the drops inside the spray can be obtained. These data give an indication of the areas in the spray where large drop velocities and/or large drop diameters are present, resulting in more energetic impingements at and larger cavities inside the target surface film during spray impingement. In this thesis, only the vertical velocity components of the drops are taken into account, as it is expected that the kinetic energies defined by the vertical velocity magnitude of the spray drops are mostly responsible for the fluctuating surface film, the radial film velocity components and the time evolution of the cavities appearing inside this film. It has to be noted that the PDA-measurements are conducted in the free spray, hence without taking into account the impingement process. This means that the influences of the impinging spray on the spray characteristics, like the velocity and diameter distribution of the spray before impingement, are not taken into account. This can be justified by the fact that a very fine spray is used, due to which the influence of the impingement process on the spray characteristics is assumed to be small.

Mean vertical drop velocities

Figure 7.2 presents some exemplary results of the distributions of the mean vertical velocity magnitudes of the drops inside the spray at two different horizontal planes inside the spray for different volume flows of the US10-nozzle.

In this figure the black interrupted circle corresponds to the diameter of the mean spray cone, obtained by the shadowgraphy measurements presented in the paragraph above. All the measurements presented in this figure are obtained by applying the nozzle with the pressurized air at 0.604 bar overpressure in order to stabilize the spray cone.

In this figure it can be seen that for most of the volume flows at both horizontal planes inside the spray the areas with high mean drop velocities are centered around the rotational axis of the spray cone. For the volume flows of 100 mL/min to 200 mL/min this area with higher mean drop velocities is increasing in size between the upper and the lower investigated horizontal planes, as is to be expected, since the spray cone is increasing in size for increasing distance from the nozzle, Figure 7.1. However, the maximum measured values for the drop mean velocities are higher for the upper horizontal plane, as here the drops in the spray have experienced the air drag forces for a shorter time. The values of the mean vertical drop velocities at both investigated planes and for both nozzles are shown as a function of the volume flow in Figure 7.3, together with the curves fitted through the measurements. A small difference in spray vertical velocities between the upper and lower horizontal planes is found.

An increase in volume flow has a clear effect on the vertical velocity magnitudes of the spray for both nozzles, hence at both investigated horizontal planes the area and magnitudes of the velocities increase for increasing volume flow. In Figure 7.3 the values of the mean vertical drop velocities at both investigated planes for both nozzles are shown as a function of the volume flow.

A clear linear dependency is found, meaning that the vertical drop velocities increase linearly with increasing nozzle volume flow. This is the direct result of the continuity equation applied at the nozzle exit. Due to an increased volume flow and equal nozzle exit areas, the velocity of the spray leaving the nozzle has to increase, resulting in increased velocity magni-

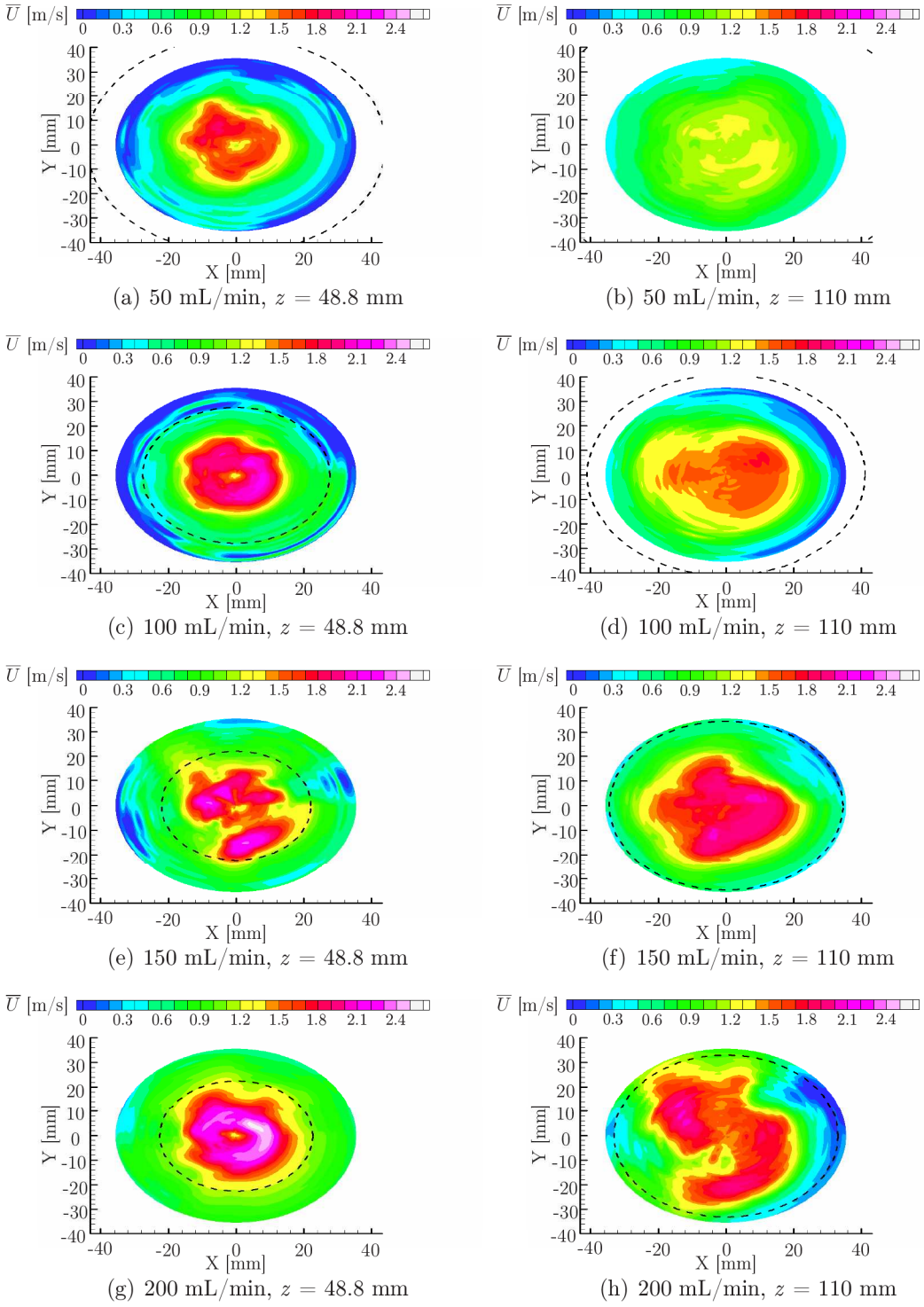

(a) 50 mL/min, $z = 48.8$ mm

(b) 50 mL/min, $z = 110$ mm

(c) 100 mL/min, $z = 48.8$ mm

(d) 100 mL/min, $z = 110$ mm

(e) 150 mL/min, $z = 48.8$ mm

(f) 150 mL/min, $z = 110$ mm

(g) 200 mL/min, $z = 48.8$ mm

(h) 200 mL/min, $z = 110$ mm

Figure 7.2: Mean vertical spray velocities for the ultrasonic US10 nozzle, applied with pressurized air at 0.604 bar, for different volume flows between 50 mL/min and 200 mL/min at the axial positions $z = 48.8$ mm (left) and $z = 110$ mm (right)

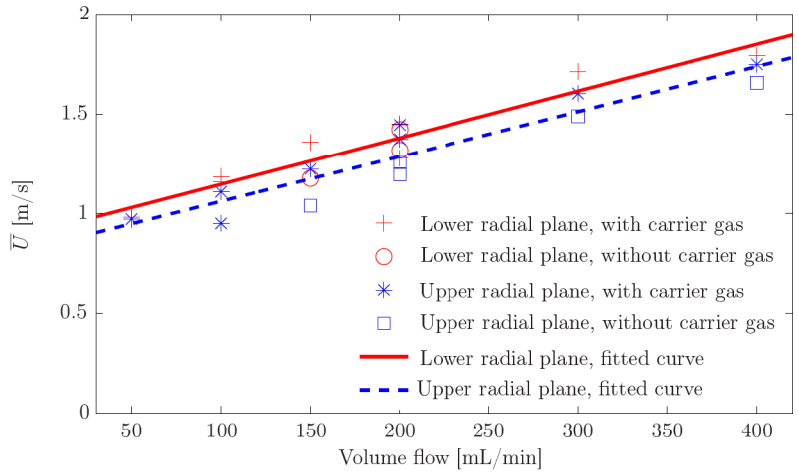

Figure 7.3: Mean vertical spray velocity vs. nozzle volume flow for US10 and US20 ultrasonic nozzle, at both investigated horizontal planes, with and without applied carrier gas

tudes of the drops at the two investigated horizontal planes.

Distributions of the Sauter mean diameter of the sprays

It is well-known that different mean values for the drop sizes can characterise the drop sizes in the spray. Among others, like the mean length (D_{10}), mean surface area (D_{20}) or mean volume (D_{30}) of the drops, the Sauter mean diameter (D_{32}) is commonly used. This Sauter mean diameter is defined as the mean volume-to-surface ratio for all droplets of the spray and can be seen as the mean diameters of the drops, having the same volume-to-surface ratio as the entire spray at a certain position. The general definition is given by

$$SMD = D_{32} = \frac{\sum_{i=1}^{N} \Delta N_i d_{pi}^3}{\sum_{i=1}^{N} \Delta N_i d_{pi}^2} \tag{7.1}$$

and gives an indication of the mass distribution of the drops inside the spray.

In Figure 7.4 the Sauter mean diameter distributions of the spray for different volume flows at the two investigated heights inside the spray are presented, as an example, for the US10-nozzle. For all investigated volume flows a clear area, situated at the inner core of the spray, is found, where small values of the Sauter mean diameters, up to about $D_{32} = 150\ \mu m$, are present. These inner cores with relatively small SMD-values correlate very well with those areas, where higher mean vertical drop velocities are obtained, compare Figure 7.2 with Figure 7.4, as well as with those areas, in which the mean drop diameters are lower (not presented here). Since the mean vertical velocities are highest at these inner cores, more waviness and disturbances of the surface film are expected. Furthermore, due to the lower spray mass that is deposited onto the target surface, a thinner film will be the result. The results of the mean radial film velocity distributions are presented in §(7.2).

In the outer regions of the spray, where low mean vertical drop velocities are found, Sauter mean diameters up to $D_{32} = 280\ \mu m$ are measured. This means, that an higher amount of the spray mass is distributed at the outer regions of the spray, hence, more mass will be deposited

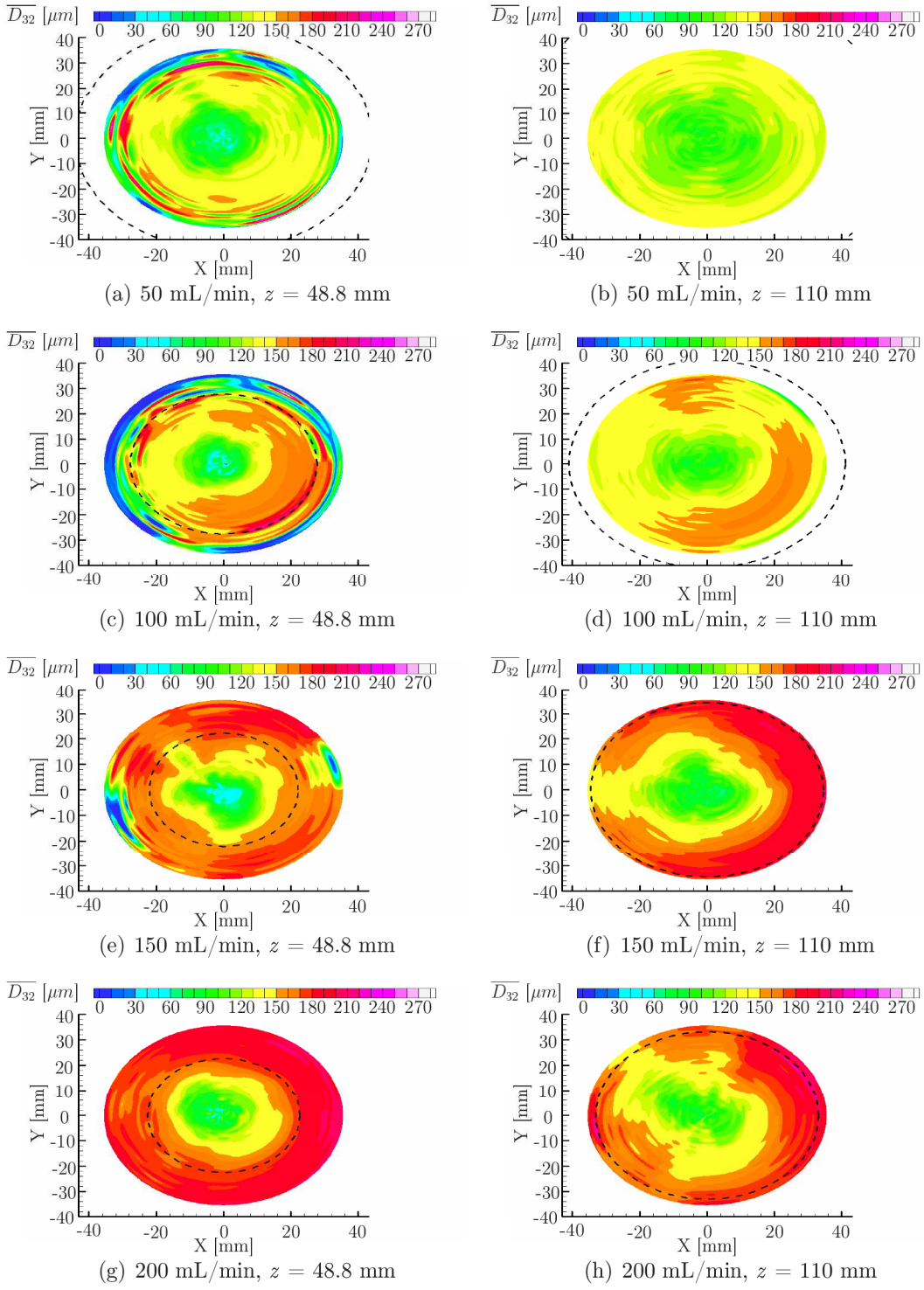

(a) 50 mL/min, z = 48.8 mm

(b) 50 mL/min, z = 110 mm

(c) 100 mL/min, z = 48.8 mm

(d) 100 mL/min, z = 110 mm

(e) 150 mL/min, z = 48.8 mm

(f) 150 mL/min, z = 110 mm

(g) 200 mL/min, z = 48.8 mm

(h) 200 mL/min, z = 110 mm

Figure 7.4: Sauter mean diameter (D_{32}) distributions for the ultrasonic US10 nozzle, applied with pressurized air at 0.604 bar, for different volume flows between 50 mL/min and 200 mL/min at the axial positions z = 48.8 mm (left) and z = 110 mm (right)

onto the outer edges of the surface film during impingement of the spray, thereby generating a thicker surface film. However, since in these regions the mean vertical drop velocities are lower, less disturbance of the film and lower radial velocities inside the film are expected at the outer impingement regions.

An increase in the volume flow has for both investigated nozzles the same effect, namely a clear increase in the areas where higher values of the Sauter mean diameter are observed, as well as an increase in the measured absolute values of the Sauter mean diameter. In Figure 7.5 the Sauter mean diameter is plotted versus the investigated volume flows for both horizontal planes inside the spray and both nozzles. In this figure it can be seen that the Sauter mean diameters between the two horizontal spray planes differ only slightly. This is due to the spray, consisting of very fine drops when leaving the nozzle. These fine drop distributions lead to almost no secondary atomization inside the spray, due to which the mass distributions of the sprays remain the same between the two different horizontal planes. A clear parabolic behaviour between the Sauter mean diameter and the volume flows is found, where the Sauter mean diameter increases up to a maximum for volume flows of about 250 - 280 mL/min. For higher volume flows, the Sauter mean diameter decreases again, since the spray changes from a full-cone spray to a hollow cone spray, leading to a distribution of the mass which is directed more to the outside regions of the spray. These changes in mass distributions introduce larger inner cores, where small Sauter mean diameters are present, therefore leading to decreases of the averaged Sauter mean diameters.

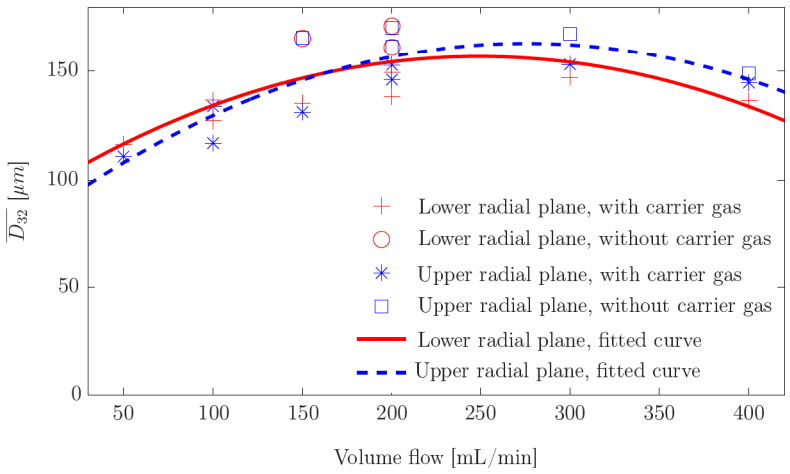

Figure 7.5: Sauter mean diameter vs. nozzle volume flow for the US10 and US20 ultrasonic nozzle, at both investigated horizontal planes, with and without applied carrier gas

Distributions of the kinetic energy of the sprays at their impingement heights

In the paragraphs above, the characterisation of the impinging spray is described by means of shadowgraphy measurements and phase-Doppler measurements. This spray characterisation is necessary for understanding the typical velocity distributions and drop diameter distributions of the spray at the different impingement heights. With these outcomes the mean kinetic energy of the sprays can be calculated. The general definition is given by

$$\overline{U_{kin}} = \frac{\rho \pi D_d^3 \overline{U_d}^2}{12} \tag{7.2}$$

and gives an indication of the vigorously with which the drops at a certain area of the spray impinge onto the surface film.

When comparing the distributions of the kinetic energies for different volume flows for the same investigated nozzle, a very clear strong increase of the kinetic energies is observed, Figure 7.6. This increase in kinetic energy is the direct effect resulting from an increase of the vertical mean drop velocities for larger volume flows.

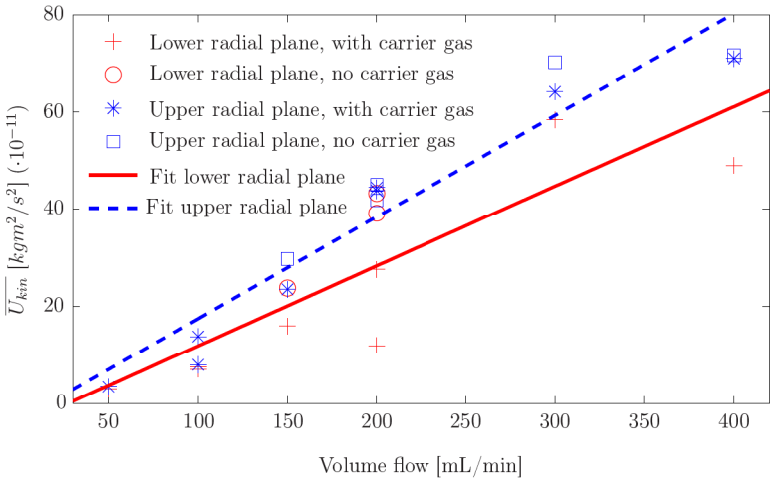

Figure 7.6: Mean kinetic energy vs. nozzle volume flow for the US10 and US20 ultrasonic nozzle, at both investigated horizontal planes, with and without applied carrier gas

Conclusively, three main physical phenomena, obtained by the *PDA*-measurements, can be summarized as direct results of a change in impingement height or a change in volume flow for both investigated ultrasonic atomizers. The inner core of each spray is defined by large values of the mean vertical drop velocities, as well as low values of the mean drop diameters and Sauter mean diameters. Due to the low drop diameters, the kinetic energies of the spray cores are relatively low.

For increasing impingement heights the regions with relatively high mean vertical drop velocities increase, but simultaneously the maximum absolute values decrease due to the influence of the air drag forces on the drops. However, no clear change in the mean drop diameters or the Sauter mean diameters is observed, due to which the kinetic energies of the sprays have to decrease for increasing impingement heights.

In case of increasing volume flow the regions where relatively high mean vertical drop velocities are measured, are increasing with a simultaneous increase in the absolute maximum values of these vertical drop velocities. At the same time, the spray drop diameters and Sauter mean diameters increase as well. Both of these phenomena lead to strong increases of the kinetic energy distributions of the sprays for both ultrasonic atomizers.

7.2 Film radial velocity distributions for spray impingement

The velocity distributions inside the surface film are of great importance, for example in spray cooling. For spray cooling, the directions and magnitudes of these velocities give an indication in which direction and how fast the heat is being transported away from the hot surface, which parts of the hot surface are being cooled less and how fast the warm liquid is being refreshed by new cold liquid. In order to obtain the radial velocity distributions and their fluctuations inside the surface film, measurements are conducted by using the adapted volumetric μ-PIV technique. The working principle of this technique, as well as the optical arrangement and the adaptation of the technique to the measurement requirements has been described in §(6.2.2).

With the adapted μ-PIV setup, three-dimensional recordings of the tracer particles motions, present inside the impinging spray and the surface film, are obtained from below the surface film. This optical system results in a spatial resolution of 8.9 $\mu m/pix$, hence, a total field of view of 11.4 $\times$ 9.1 mm per recording. One quarter of the total spray impingement region is selected to investigate the radial film velocities and their fluctuations, with a total size of 44.4 $\times$ 45.1 mm. This region is subdivided into 20 equal areas of 11.4 $\times$ 9.1 mm, hence, the field of view of the recording camera, with an overlap of 0.4 mm and 0.1 mm respectively between two subregions. To obtain reliable data for the mean velocity components and their fluctuations, 1000 tracer particle image pairs are recorded per subregion at a recording rate of 2 Hz. In this way, clear radial velocity fields are obtained at the two impingement heights for both nozzles. With the use of an image processing subroutine the 1000 instantaneous obtained vector fields for the 20 subregions for each impingement height are put together, after which the mean radial velocity fields and fluctuations can be calculated. The complete image processing algorithm has been described in §(6.2.2). Simultaneously to the surface film radial velocity measurements the film thickness of the surface films is recorded by a second camera. It is observed that for all volume flows, at both impingement heights and for both ultrasonic nozzles the mean film thickness varies between 1.45 and 1.55 mm, meaning the results of spray impingement on deep pools are shown hereafter. The fluctuations of the film thicknesses are in the order of about 100 μm.

7.2.1 Mean radial film velocities

The mean radial velocity distributions inside the surface films at the two investigated impingement heights are shown in the Figures 7.7 and 7.8 for, respectively, the ultrasonic nozzles US10 and US20, both applied with pressurised air as the carrier gas, as well as in Figure 7.9 for both ultrasonic nozzles, without using the carrier gas to stabilize the spray. In these figures, the left columns correspond to the upper radial planes, hence a lower impingement height, whereas the right columns are the mean velocity fields for higher impingement heights. **Note**: the mean radial velocity distributions are obtained by integrating over the total height of the surface films.

In these figures the background colors define the magnitudes of the mean radial film velocities, whereas the white lines represent the streamlines. As was mentioned above, each of these figures is build up out of 20 subregions, recorded subsequently with a temporal space of about 30 minutes, due to which in some figures the mean radial velocity magnitudes show some jumps in value going from one subregion to another. Although the time span inbetween the first and the last of the 20 subregions is about 10 hours, a clear mean velocity field is obtained for almost all volume flows for both nozzles.

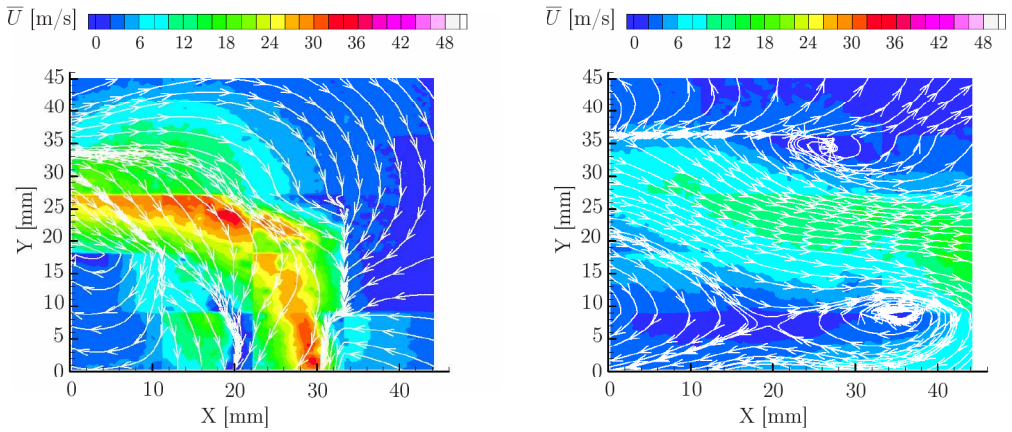

(a) 100 mL/min, $z = 48.8$ mm (b) 100 mL/min, $z = 110$ mm

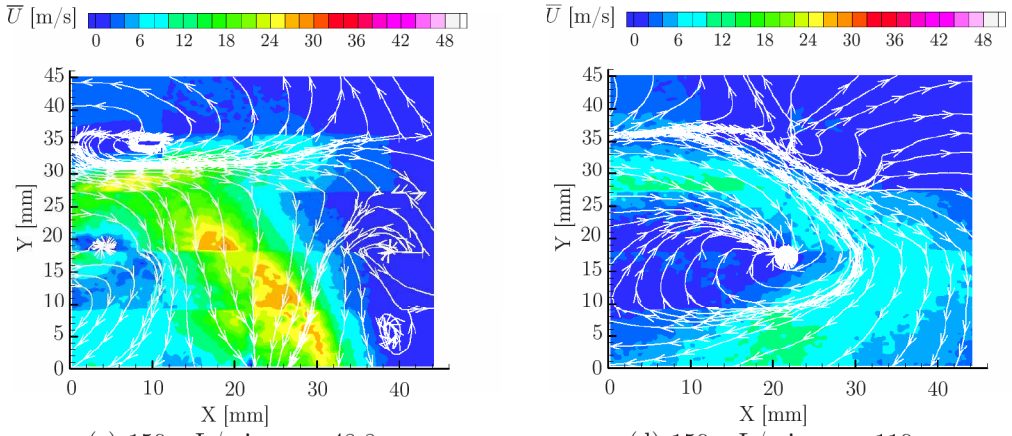

(c) 150 mL/min, $z = 48.8$ mm (d) 150 mL/min, $z = 110$ mm

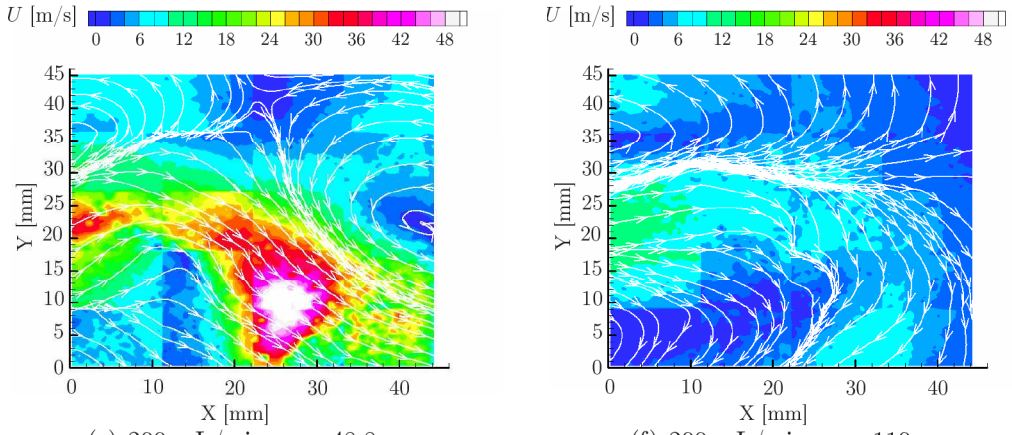

(e) 200 mL/min, $z = 48.8$ mm (f) 200 mL/min, $z = 110$ mm

Figure 7.7: Mean radial surface film velocities for impingement of a spray, generated by the ultrasonic US10 nozzle, applied with pressurized air at 0.604 bar, for different volume flows between 100 mL/min and 200 mL/min at the axial positions $z = 48.8$ mm (left) and $z = 110$ mm (right)

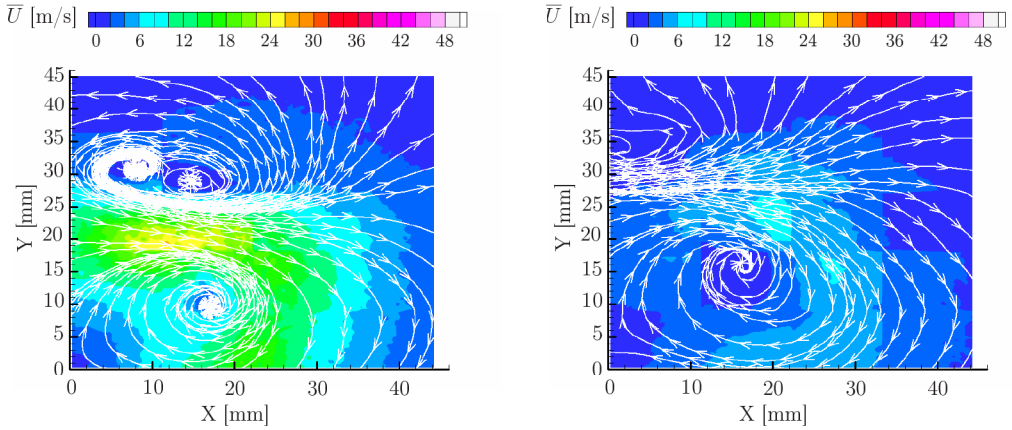

(a) 100 mL/min, $z = 61.3$ mm (b) 100 mL/min, $z = 122.5$ mm

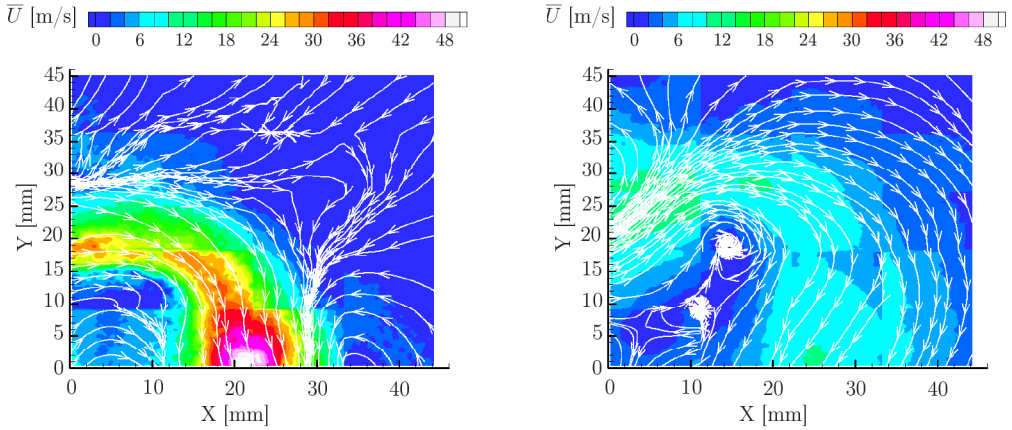

(c) 200 mL/min, $z = 61.3$ mm (d) 200 mL/min, $z = 122.5$ mm

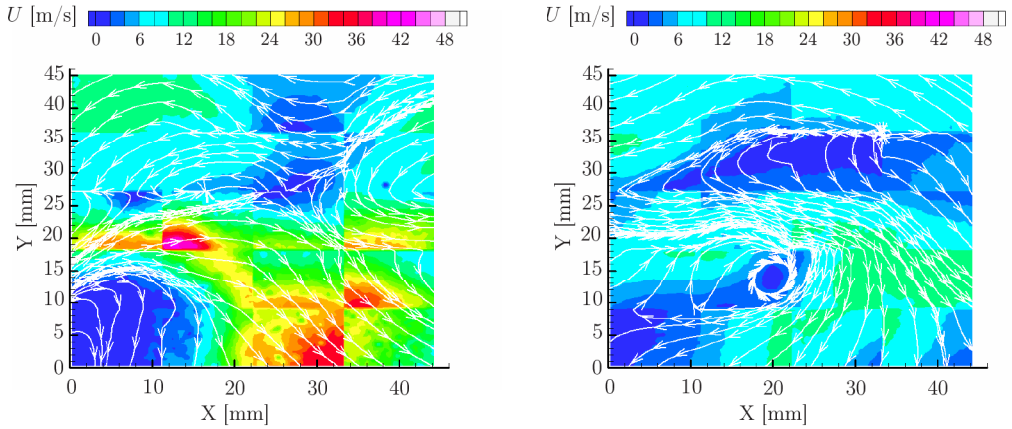

(e) 300 mL/min, $z = 61.3$ mm (f) 300 mL/min, $z = 122.5$ mm

Figure 7.8: Mean radial surface film velocities for impingement of a spray, generated by the ultrasonic US20 nozzle, applied with pressurized air at 0.604 bar, for different volume flows between 100 mL/min and 300 mL/min at the axial positions $z = 61.3$ mm (left) and $z = 122.5$ mm (right)

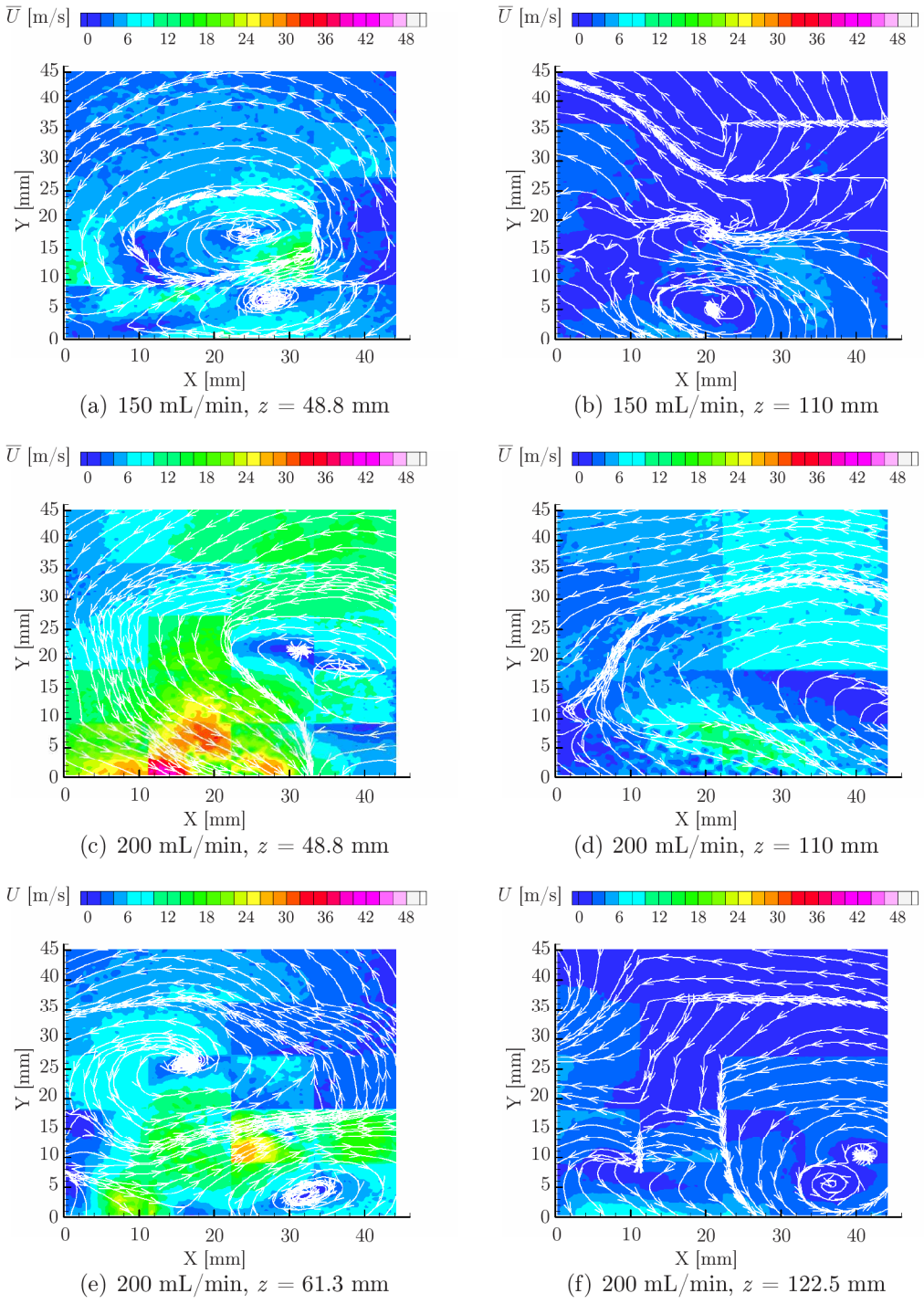

(a) 150 mL/min, $z = 48.8$ mm

(b) 150 mL/min, $z = 110$ mm

(c) 200 mL/min, $z = 48.8$ mm

(d) 200 mL/min, $z = 110$ mm

(e) 200 mL/min, $z = 61.3$ mm

(f) 200 mL/min, $z = 122.5$ mm

Figure 7.9: Mean radial surface film velocities for impingement of a spray, generated by the ultrasonic US10 (a-d) and US20 (e-f) nozzles, without carrier gas, for two different volume flows of 150 mL/min and 200 mL/min at the axial positions $z = 48.8$ mm (left) and $z = 110$ mm (right) for US10 and at $z = 61.3$ mm (left) and $z = 122.5$ mm (right) for US20

Several interesting observations can be made when comparing the obtained mean radial film velocity fields. For every recording, the mid-point of the nozzle exit is positioned at (x, y) = (0, 0), but due to the inclined core of the sprays for most investigated volume flows, the centers of the sprays for most recordings do not lie at this coordinate, but are shifted in the direction of the spray inclination, see for example Figures 7.8(a) and 7.8(b). Looking at the streamline patterns, it is observed that the swirling motion of the spray, given to the spray by the nozzle when exiting the nozzle, is passed on to the motion of the surface film. This comes clearly forward in the large vortices present in the surface films at both investigated impingement heights for both nozzles. The centers of these large vortices correspond to the centers of the impinging sprays. What is interesting to note is that all sprays, obtained for both nozzles using the carrier gas, as well as the corresponding vortices inside the surface films are rotating in clockwise direction for both impingement heights, whereas the surface film vortices for impinging sprays without carrier gas are rotating in an anticlockwise sense (Figure 7.9), meaning that the carrier gas changes the swirl direction of the spray.

An increase in the impingement height of the sprays results in a clear decrease of the mean radial film velocities, as a result of the decrease of the mean vertical velocity of the sprays and the subsequent decrease of the kinetic energy. Therefore the energy with which the drops of the spray impinge onto the liquid surface is smaller, hence smaller cavities appear inside the surface film, resulting in a decrease of the radial film velocities induced by these cavities. However, the size of the areas where mean radial film velocities larger than $\overline{U} = 0.6$ m/s are present increases, which is in line with the radial expansion of the spray cones for increasing impingement heights. The directions of the streamlines show no correlation at all between the two impingement heights; the same is found for the size and strength of the surface film vortices.

No clear dependency of an increase in volume flow on the surface film mean radial velocity directions is found for both impingement heights and both nozzles. In some films several counter-rotating vortices are observed, for example Figure 7.8(a) and Figure 7.9(e), whereas for other volume flows only one strong vortex is measured. For larger volume flows the areas with relatively high mean radial film velocities, as well as the values of the maximum absolute radial film velocities, are increasing, since an increase in volume flow is directly linked to an increase in the kinetic energy of the drops of the spray, Figure 7.6. Due to this larger kinetic energy, the sprays introduce at impingement larger cavities in the surface film, resulting in larger radial film velocities. These increasing areas with larger mean radial film velocities for both impingement heights and for most investigated volume flows correspond quite well with the borders of the spray cores where relatively large mean vertical drop velocities are found, Figures 7.2.

In general it can be said that the sprays, generated by the two investigated ultrasonic nozzles US10 and US20, introduce random mean surface film movements and velocities, which are quite distinct at different impingement heights and volume flows.

7.2.2 Radial film velocity fluctuations

The surface film, generated by an impinging spray is constantly fluctuating by the subsequent and simultaneous impingement of multiple drops of the spray, having different kinetic energies. These film fluctuations are seen in the form of fluctuating heights of the film, waves appearing on the surface of the film and fluctuating radial film velocities. The amount and strengths of

the fluctuations are based on the kinetic energy distributions in the spray, and may differ severely depending on the position inside the impingement area.

By measuring the instantaneous film velocity distributions over a longer time, the fluctuations in the radial film velocities can be made visible. The turbulence intensity distributions, calculated by eq. (6.17), are shown in Figure 7.10 and 7.11 for, respectively, nozzle US10 and US20, both applied with carrier gas, for different volume flows and for the two investigated impingement heights. In Figure 7.12, the turbulence intensity distributions for both nozzles, without carrier gas, are shown. In these figures the background colors define the absolute values of the turbulence intensities, whereas the arrows show the directions of the mean radial film velocities. These figures show that at most positions in the film the turbulence intensities for all investigated volume flows at both impingement heights lie below $TI = 0.75{\cdot}\overline{U_{film}}$. Values lower than $TI = 0.5{\cdot}\overline{U_{film}}$ correlate exactly with locations in the surface film where relatively high mean radial film velocities are observed. This correlation is clearly seen when comparing the left images of Figures 7.7 and 7.8 with, respectively, the left images of Figures 7.10 and 7.11. In the latter two figures, clearly the elliptical and spherical shapes of the areas with relatively low turbulence intensities, hence relatively high mean radial film velocities, can be pointed out easily. Higher values of the turbulence intensities, up to $TI = 5{\cdot}\overline{U_{film}}$, are found at the positions of vortex cores and at saddle points, where the film velocities are fluctuating strongly in direction and magnitude. No correlation is found between the different turbulence intensity distributions for increasing volume flows or for increasing impingement heights, hence, an decrease in kinetic energy of the impinging spray for higher impingement heights has no large influence on the radial velocity fluctuations of the surface film.

Appendix D presents the non-dimensional film velocity fluctuations in both in-plane directions, $u'/\overline{U}_{film}$ and $v'/\overline{U}_{film}$, as well as the Reynolds tensions, $u'v'/\overline{U}_{film}$. When comparing the film velocity fluctuations in both directions, it is found that the areas with relatively low values of the velocity fluctuations differ, but those where high velocity fluctuations, up to $TI = 5{\cdot}\overline{U_{film}}$, are situated are similar in size, magnitude and position. These distributions are directly linked to the mean velocity distributions of the surface film. Areas where the flow is mainly in one of both directions, show higher velocity fluctuations in this particular direction, whereas at the positions of saddle points and vortex cores the fluctuations in both directions are strong, since at these particular points the flow direction changes sharply from one instantaneous recording to the next.

7.3 Summary

In this chapter the results of the spray impingement measurements have been presented in detail. The sprays, produced by two ultrasonic nozzles US10 and US20 of Lechler GmbH, have been investigated for volume flows of 50 mL/min to 200 mL/min at two impingement heights of 48.8 mm and 110 mm for US10, as well as for volume flows between 100 mL/min and 400 mL/min at two impingement heights of 61.3 mm and 122.5 mm for US20. The sprays of both nozzles, applied with and without pressurized air at 0.6 bar overpressure, have been measured. The presentation of the results was split up into two main parts; the first part focussed on the characterisation of the spray by means of *PDA*, hence, the distribution of the drop diameters, drop mean vertical velocities, mass distribution and kinetic energy distribution of the impinging sprays. The second part focussed on the mean velocity distributions and velocity fluctuations, obtained by $\mu - PIV$, inside the surface film, which appeared on the solid surface for spray impingement.

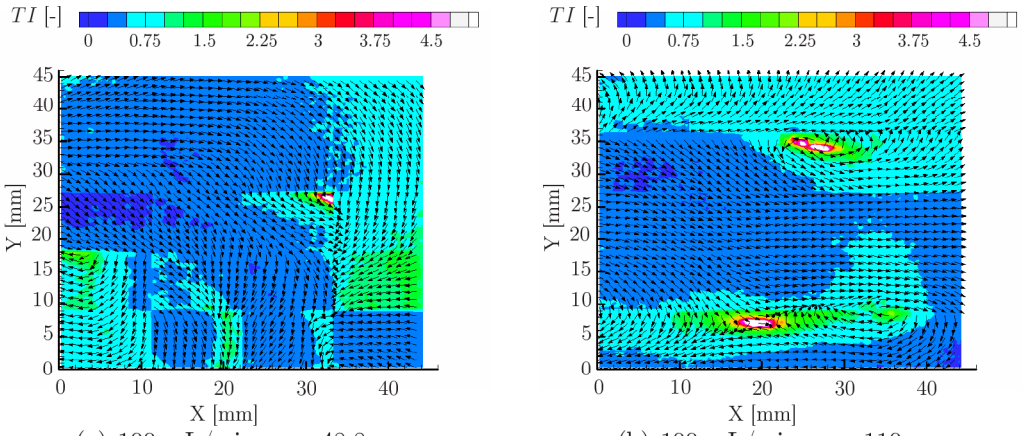

(a) 100 mL/min, $z = 48.8$ mm (b) 100 mL/min, $z = 110$ mm

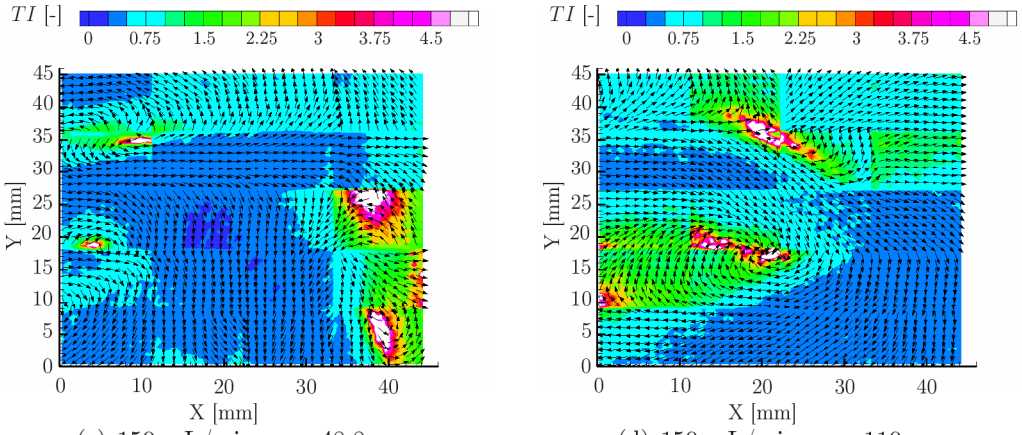

(c) 150 mL/min, $z = 48.8$ mm (d) 150 mL/min, $z = 110$ mm

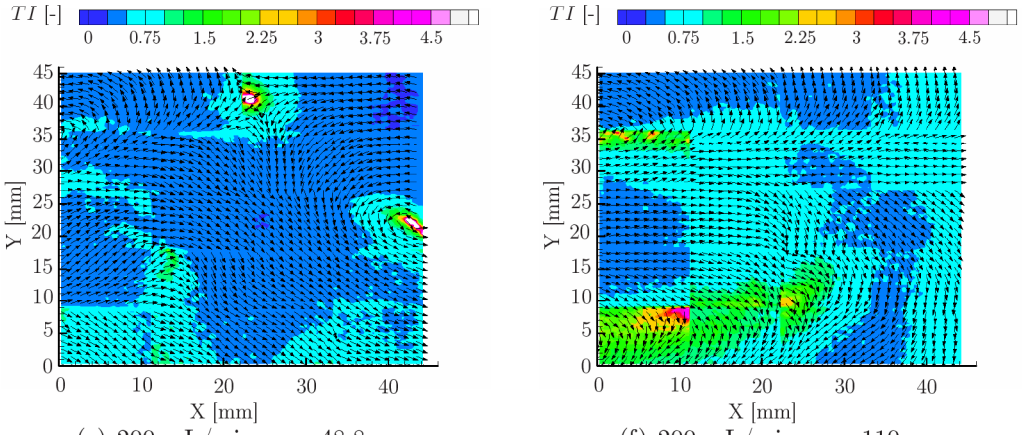

(e) 200 mL/min, $z = 48.8$ mm (f) 200 mL/min, $z = 110$ mm

Figure 7.10: Radial turbulence intensity fields inside the surface film for impingement of a spray, generated by the ultrasonic US10 nozzle, applied with pressurized air at 0.604 bar, for different volume flows between 100 mL/min and 200 mL/min at the axial positions $z = 48.8$ mm (left) and $z = 110$ mm (right)

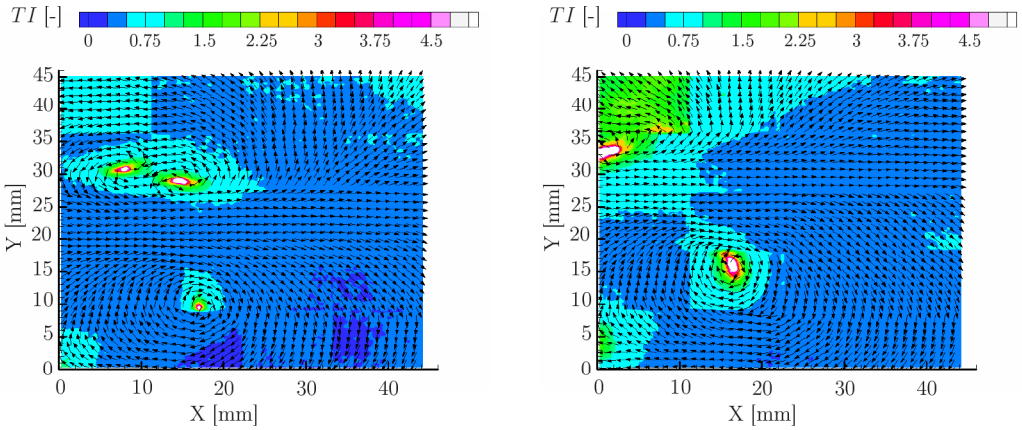

(a) 100 mL/min, $z = 61.3$ mm (b) 100 mL/min, $z = 122.5$ mm

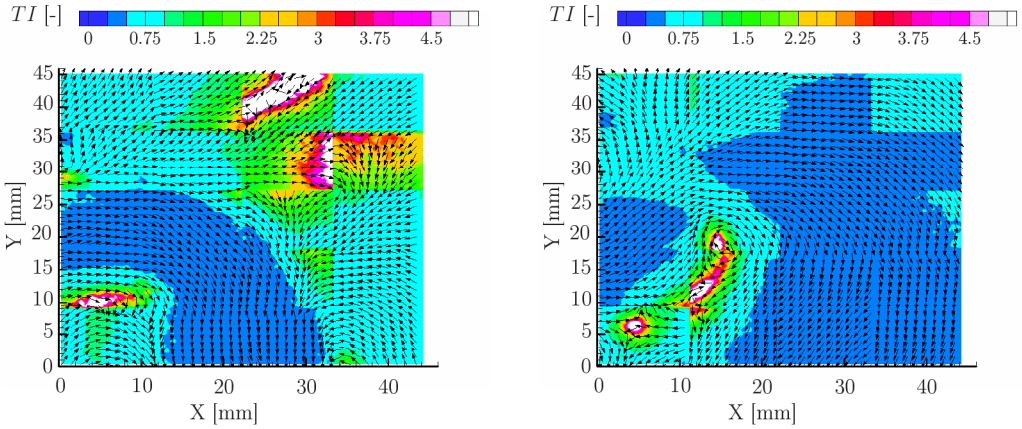

(c) 200 mL/min, $z = 61.3$ mm (d) 200 mL/min, $z = 122.5$ mm

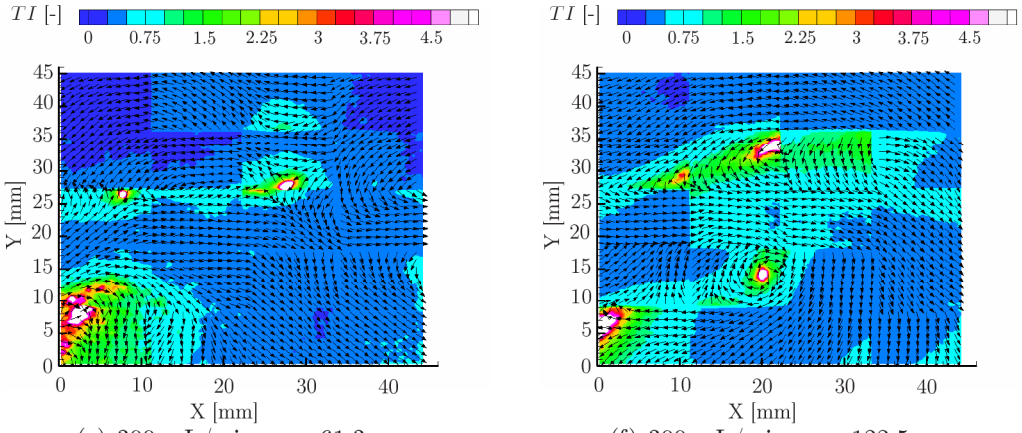

(e) 300 mL/min, $z = 61.3$ mm (f) 300 mL/min, $z = 122.5$ mm

Figure 7.11: Radial turbulence intensity fields inside the surface film for impingement of a spray, generated by the ultrasonic US20 nozzle, applied with pressurized air at 0.604 bar, for different volume flows between 100 mL/min and 300 mL/min at the axial positions $z = 61.3$ mm (left) and $z = 122.5$ mm (right)

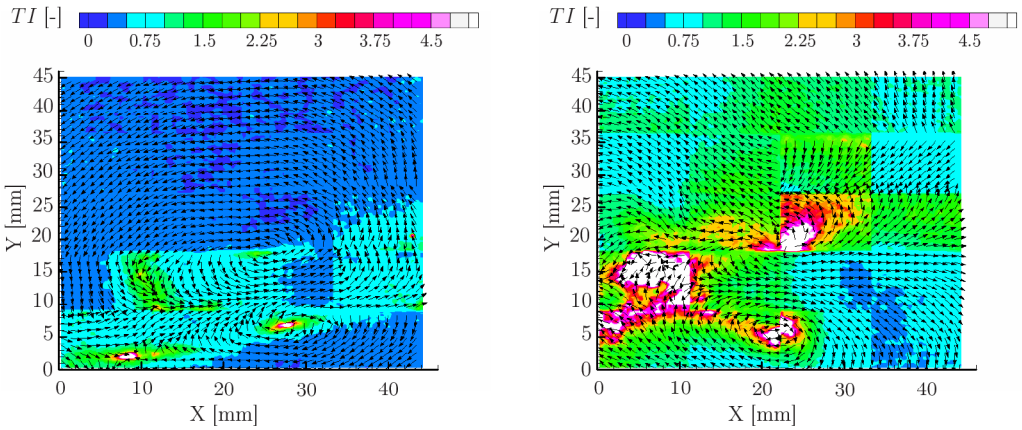

(a) 150 mL/min, $z = 48.8$ mm

(b) 150 mL/min, $z = 110$ mm

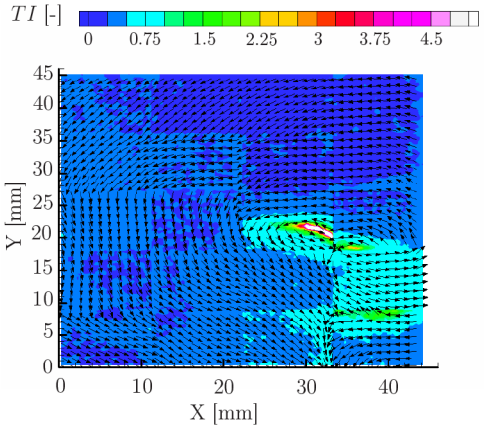

(c) 200 mL/min, $z = 48.8$ mm

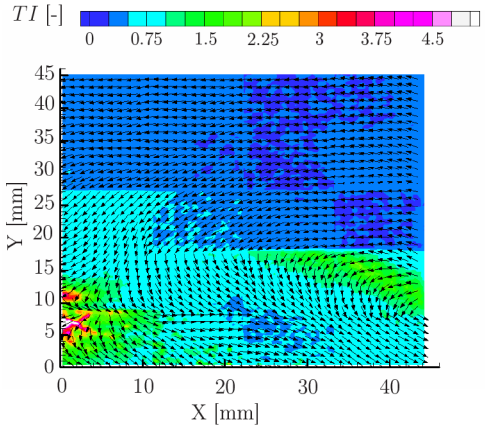

(d) 200 mL/min, $z = 110$ mm

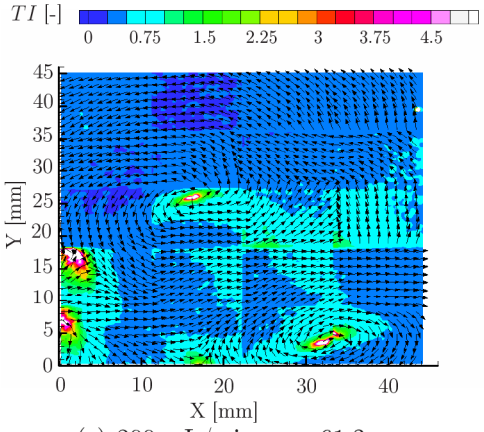

(e) 200 mL/min, $z = 61.3$ mm

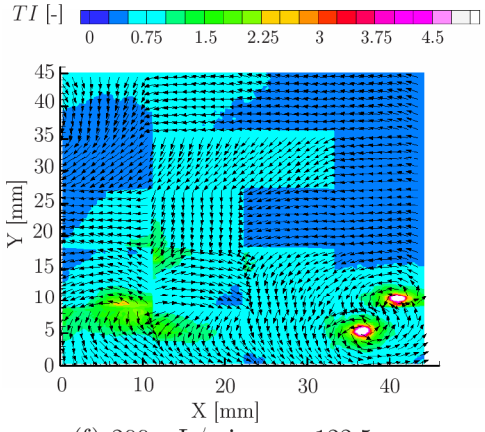

(f) 200 mL/min, $z = 122.5$ mm

Figure 7.12: Radial in-plane turbulence intensity fields of the surface film for spray impingement, generated by the ultrasonic US10 (a-d) and US20 (e-f) nozzles, without carrier gas, for two different volume flows of 150 mL/min and 200 mL/min at the axial positions $z = 48.8$ mm (left) and $z = 110$ mm (right) for US10 and at $z = 61.3$ mm (left) and $z = 122.5$ mm (right) for US20